Gravitationally lensed quasars and supernovae in future wide-field optical imaging surveys

Masamune Oguri[1,2]* and Philip J. Marshall[2,3]

[1]*Division of Theoretical Astronomy, National Astronomical Observatory of Japan, 2-21-1 Osawa, Mitaka, Tokyo 181-8588, Japan.*
[2]*Kavli Institute for Particle Astrophysics and Cosmology, Stanford University, 2575 Sand Hill Road, Menlo Park, CA 94025, USA.*
[3]*Physics Department, University of California, Santa Barbara, CA 93601, USA.*

7 August 2011

ABSTRACT
Cadenced optical imaging surveys in the next decade will be capable of detecting time-varying galaxy-scale strong gravitational lenses in large numbers, increasing the size of the statistically well-defined samples of multiply-imaged quasars by two orders of magnitude, and discovering the first strongly-lensed supernovae. We carry out a detailed calculation of the likely yields of several planned surveys, using realistic distributions for the lens and source properties and taking magnification bias and image configuration detectability into account. We find that upcoming wide-field synoptic surveys should detect several thousand lensed quasars. In particular, the Large Synoptic Survey Telescope (LSST) should find more than some 8000 lensed quasars, some 3000 of which will have well-measured time delays. The LSST should also find some 130 lensed supernovae during the 10-year survey duration, which is compared with ~ 15 lensed supernovae predicted to be found by a deep, space-based supernova survey done by the Joint Dark Energy Mission (JDEM). We compute the quad fraction in each survey, predicting it to be $\sim 15\%$ for the lensed quasars and $\sim 30\%$ for the lensed supernovae. Generating a mock catalogue of around 1500 well-observed double-image lenses, as could be derived from the LSST survey, we compute the available precision on the Hubble constant and the dark energy equation parameters for the time delay distance experiment (assuming priors from Planck): the predicted marginalised 68% confidence intervals are $\sigma(w_0) = 0.15$, $\sigma(w_a) = 0.41$, and $\sigma(h) = 0.017$. While this is encouraging in the sense that these uncertainties are only 50% larger than those predicted for a space-based type-Ia supernova sample, we show how the dark energy figure of merit degrades with decreasing knowledge of the the lens mass distribution.

Key words: cosmological parameters — cosmology: theory — gravitational lensing

1 INTRODUCTION

The discovery of strong gravitational lensing in Q0957+561 (Walsh et al. 1979) opened up the possibility of using strong lens systems to study cosmology and astrophysics. Roughly a few hundred strong lens systems produced by massive galaxies have been discovered to date, with quasars (e.g., Inada et al. 2008), radio sources (e.g., Myers et al. 2003; Browne et al. 2003), and galaxies (e.g., Cabanac et al. 2007; Faure et al. 2008; Bolton et al. 2008) appearing as source populations. These samples of strong lenses have been extensively used to constrain dark energy, the density profile of lensing galaxies, and the evolution of massive ellipticals (see, e.g., Kochanek 2006, for a review).

It is expected that large new samples of strong lenses will be obtained in future wide-field imaging surveys (e.g., Kuhlen et al. 2004; Marshall, et al. 2005). For instance, the Large Synoptic Survey Telescope (LSST; Ivezić et al. 2008) will observe a 20,000 deg^2 region with a final limiting magnitude of $r \sim 27.5$, which is considerably wider and deeper than existing optical imaging surveys such as the Sloan Digital Sky Survey (SDSS; York et al. 2000). More importantly, future imaging surveys such as LSST's will pay particular attention to the acquisition of time-domain data, mostly in order to study transient objects including supernovae (SNe).

In this paper, we present detailed predictions of the numbers of time-variable sources we can expect to be strongly lensed in ongoing and future time domain optical imaging surveys. We focus on time-variable sources for two reasons. First, time domain data enable us to identify strong lenses by taking advantage of time variability (Pindor 2005). Kochanek et al. (2006) proposed to find strong lenses

* E-mail: masamune.oguri@nao.ac.jp

by looking for "extended variable sources" in time-domain data, and argued that this technique should be very efficient due to the low levels of contamination in the difference images. Second, time-variable sources allow us to measure time delays between multiple images; these time delays contain rich information on the lens potentials as well as cosmology (e.g., Witt et al. 2000; Kochanek 2002; Saha & Williams 2003; Schechter 2005; Oguri 2007a; Congdon et al. 2008, 2010; Keeton & Moustakas 2009; Keeton 2010).

The obvious and traditional example of such a strongly lensed time-variable source is a quasar (QSO). Of ~ 100 gravitationally lensed quasars currently known, time delays have been measured for only $\lesssim 20$ (see Oguri 2007a, for a recent compilation). A major advance offered by the upcoming imaging surveys is their potential not only to discover new lenses but also monitor them as well. Some of the survey telescopes we will consider do have larger static surveys planned, but we do not consider them on the grounds that if they are wide enough to be competitive, they will be limited by the required monitoring follow-up. Synoptic surveys (such as those designed to discover supernovae) should provide some estimate of the lens time delays – we are careful to point out where this may not be the case.

The scope of several planned surveys allows us also to consider SNe as time-variable sources. While a distant SN highly magnified by a foreground massive cluster has recently been identified (Stanishev et al. 2009; Goobar et al. 2009), no multiply-imaged SN has yet been discovered. However, the possibility of discovering such strongly-lensed SNe by future time-domain surveys such as the Joint Dark Energy Mission (JDEM) and the LSST has been pointed out (Porciani & Madau 2000; Holz 2001; Goobar et al. 2002; Oguri et al. 2003; Mörtsell et al. 2005). A particularly enticing feature of lensed SNe is that, if they are type-Ia, the "standardizable candle" nature of the peak brightness allows a direct determination of the lensing magnification factor, which breaks the degeneracy between the lens potential and the Hubble constant (Oguri & Kawano 2003).

Indeed, we expect any large sample of time delay lenses to be useful in constraining cosmological parameters. The idea of using strong gravitational lens systems with time-variable sources to measure the Hubble constant is an old one (Refsdal 1964); in fact, the time delays between images provide a way of measuring the "time-delay distance" to the lens. This quantity is a combination of the angular diameter distances to the lens, source, and between the two, and while primarily sensitive to H_0, it does also depend on the other cosmological parameters (see e.g., Suyu et al. 2010, for a recent high-precision measurement). Attempts to measure the Hubble constant from the statistical analysis of the current lensed quasar sample (Saha et al. 2006; Oguri 2007a; Coles 2008) have yielded values consistent with constraints from other cosmological probes (e.g., Freedman et al. 2001; Bonamente et al. 2006; Komatsu et al. 2009; Riess et al. 2009). In future, larger samples covering a wide range of lens and source redshift permutations should provide interesting constraints on the dark energy equation of state as well as Hubble constant (Lewis & Ibata 2002; Linder 2004; Dobke et al. 2009; Coe & Moustakas 2009). In this work, we revisit the forecast constraints on dark energy parameters for the LSST, using new, realistic predicted distributions of strong lenses.

This paper is organised as follows. In Section 2 we describe the ingredients of our lens abundance calculation, including our assumptions about both the lens and source populations. We then present our predictions for various survey depths and areas in Section 3. We then present Monte Carlo realisations of some fiducial survey lens catalogues in Section 4, and use these to explore the potential of some of these in constraining cosmological parameters via the time delay distances to the lenses in Section 5. After a brief discussion (Section 6) we conclude in Section 7. We take as the parameters of a fiducial cosmological model $\Omega_{\mathrm{m}} = 0.26$, $\Omega_{\mathrm{DE}} = 0.74$, $h = 0.72$, $w_0 = -1$ and $w_{\mathrm{a}} = 0$. We denote the angular diameter distance from observer to lens as D_{l}, from observer to source as D_{s}, and from lens to source as D_{ls}.

2   PREDICTING THE NUMBERS OF LENSED QUASARS AND SUPERNOVAE

We compute the expected number of strong lensing in future surveys in the usual way, integrating the lensing cross section of each galaxy over the galaxy population and redshift (e.g., Turner et al. 1984). As source objects, we consider both QSOs and SNe, for which measurements of time delays between multiple images will be possible due to their time-variable nature.

2.1   The population of lensing galaxies

An appropriate modeling of the lens galaxy population constitutes an essential part of the prediction for lensing rates. We mostly follow the model used in Oguri et al. (2008) to compute the expected number of strong lensing by massive galaxies in future surveys. Throughout the paper we conservatively consider only elliptical galaxies (E/S0) as lensing objects; these likely comprise $\sim 80\%$ of the total lensing probability (Turner et al. 1984; Fukugita et al. 1992; Kochanek 1996; Chae 2003; Oguri 2006; Möller et al. 2007). We assume that the mass distribution of each elliptical galaxy is described by a Singular Isothermal Ellipsoid (SIE), whose convergence is given by

$$\kappa(x,y) = \frac{\theta_{\mathrm{Ein}}}{2} \frac{\lambda(e)}{\sqrt{(1-e)^{-1}x^2 + (1-e)y^2}}, \qquad (1)$$

$$\theta_{\mathrm{Ein}} = 4\pi \left(\frac{v}{c}\right)^2 \frac{D_{\mathrm{ls}}}{D_{\mathrm{s}}}, \qquad (2)$$

where v is the one-dimensional velocity dispersion of the lensing galaxy. It has been shown that this model describe the mass distributions of observed strong lensing elliptical galaxies very well (Rusin & Ma 2001; Treu & Koopmans 2004; Rusin & Kochanek 2005; Koopmans et al. 2006, 2009; Gavazzi et al. 2007). The parameter $\lambda(e)$, the so-called dynamical normalisation, is related to the three-dimensional shape of lensing galaxies. Following Chae (2003), we assume that there is an equal number of oblate and prolate galaxies, and adopt the average value of the normalisations in each of the oblate and prolate cases. As in Oguri et al. (2008), we assume a Gaussian distribution for the ellipticity e, with a mean of 0.3 and dispersion of 0.16. The distribution is truncated at $e = 0$ and $e = 0.9$.

In addition to the SIE model lens galaxy, we include

external shear to account for the effect of the lens environment (e.g., Kochanek 1991; Witt & Mao 1997; Keeton et al. 1997). The lens potential of external shear is given by

$$\phi(x,y) = \frac{\gamma}{2}(x^2 - y^2)\cos 2\theta_\gamma + \gamma xy \sin 2\theta_\gamma. \qquad (3)$$

We assume the magnitude of the external shear, γ, follows a log-normal distribution with mean 0.05 and dispersion 0.2 dex, which is broadly consistent with the level of external shear expected from ray-tracing in N-body simulations (Holder & Schechter 2003; Dalal & Watson 2004). The orientation of the external shear, θ_γ, is assumed to be random. Although the external convergence (e.g., Oguri et al. 2005) is also vital particularly for time delays, we do not include it explicitly in the calculation. Instead, we will later consider its effects via an effective lens density profile slope, which will be the subject of detailed discussion.

For the velocity function of early-type galaxies, we adopt that derived from the SDSS data (Choi et al. 2007), which is fitted by a modified Schechter function of the following form:

$$\frac{dn}{dv} = \phi_*\left(\frac{v}{v_*}\right)^\alpha \exp\left[-\left(\frac{v}{v_*}\right)^\beta\right]\frac{\beta}{\Gamma(\alpha/\beta)}\frac{dv}{v}. \qquad (4)$$

Here, $(\phi_*, v_*, \alpha, \beta) = (8.0 \times 10^{-3} h^3 \mathrm{Mpc}^{-3}, 161\,\mathrm{km\,s}^{-1}, 2.32, 2.67)$. We do not include redshift evolution, i.e., we apply the mass distribution and velocity function to galaxies at any redshifts. Such a non-evolving model has been shown to reproduce the abundance of strong lenses in the latest radio (Chae 2007) and optical (Oguri et al. 2008) lens surveys, although see, e.g., Mitchell et al. (2005) for an analysis that takes evolution into account.

2.2 Lensing rates

The lensing probability for a given source at redshift z_s and with luminosity L is given by

$$p = \int_{\theta_{\min}}^{\theta_{\max}} d\theta \int_0^{z_s} dz_l \frac{c\,dt}{dz_l}(1+z_l)^3 \left[\frac{dn}{dv}\frac{dv}{d\theta}\sigma_{\mathrm{lens}}\right]_{v=v(\theta)}, \qquad (5)$$

where θ is the image separation between multiple images,[1] z_l indicates the redshift of lensing objects, and dn/dv denotes the velocity function of lensing galaxies given by equation (4). Unless otherwise specified, we adopt the minimum image separation of $\theta_{\min} = 0.5''$ and maximum image separation of $\theta_{\max} = 4''$. Although a non-negligible fraction of strong lenses have image separations larger than $4''$, such lensing is caused by groups or clusters of galaxies rather than a single massive galaxy (e.g., Oguri 2006). In this work we focus on galaxy-scale lenses (for which simple isothermal density profiles are good models), for two reasons. Firstly, they do dominate the lens abundance, which we will need to be high in order to beat down the statistical errors on the cosmological parameters. Secondly, the image positions are easier to fit with simple models, reflecting the fact that massive galaxies are older, more relaxed systems than groups

and clusters. On low mass scales, lenses with image separation less than $0.5''$ were deemed to be too difficult to measure, particularly in the ground-based surveys. Indeed, when we consider the yields of specific surveys below, we take into account the predicted image quality explicitly.

The lensing cross section σ_{lens} is determined by the structure of the lens potential. As discussed in §2.1, we adopt an SIE plus external shear as the lens potential of each galaxy. To take account of the magnification bias, we compute the biased cross section (Huterer et al. 2005) as follows:

$$\sigma_{\mathrm{lens}} = \int \frac{d\mathbf{u}}{\mu}\frac{d\Phi/dL(L/\mu)}{d\Phi/dL(L)}, \qquad (6)$$

where $d\Phi/dL$ is the source luminosity function and μ is the magnification factor. The integral is performed over the region where multiple images are generated. In practice, we compute the biased cross section numerically using Monte Carlo sampling of multiple images. We solve the lens equation using the software package GLAFIC (M. Oguri, in preparation). We compute the biased cross sections for double (two-images), quadruple (quad; four-images), and naked cusp (three-images) lenses separately in order to study the image multiplicity. For double lenses, we place a condition that the flux ratio must be larger than 0.1 and perform the integral over the region that satisfies this condition. This is because asymmetric double lenses with large flux differences are sometimes very difficult to locate in observations as a result of dynamic range problems caused by the brighter image.

The choice of the magnification factor μ depends on the way in which strong lens systems are identified in the survey data. Bearing in mind the promising variability selection techniques suggested by Pindor (2005) and Kochanek et al. (2006), we adopt the magnification factor of the fainter image for double lenses as μ. For quad and cusp lenses, we adopt the magnification factor of the third-brightest image, because the second-brightest image is sometimes located very close to the brightest image if it is produced near the fold catastrophe (where only one eigenvalue of magnification matrix is zero). The two images in a fold-configuration lens may be hard to deblend because of their small angular separation, which may result in failure to identify them as strongly lensed. Another reason is that the third brightest image tends to arrive first, a feature we will return to later (§4.3).

Once the lensing probability for a given source is computed, it is straightforward to calculate the expected strong lens abundance. We obtain the differential number distribution of strong lenses by integrating the lens probability over the source population:

$$\frac{dN}{dz_s} = \int_{-\infty}^{M_{\max}} dM \frac{d\Phi}{dM}\frac{dV}{dz_s}p, \qquad (7)$$

where p is given by equation (5) and M denotes the absolute magnitude of sources. The limiting absolute magnitude is simply converted from the magnitude limit of the survey considered. The volume factor dV/dz_s is given by

$$\frac{dV}{dz_s} = \Omega D_s^2 \frac{c\,dt}{dz_s}(1+z_s)^3, \qquad (8)$$

with Ω being the solid angle corresponding to the survey area.

---

[1] For strong lens systems with multiple images more than two, we define the image separation by the maximum separation between any pair of images.

Finally, the total number of strong lenses is

$$N = \int dz_{\rm s} \frac{dN}{dz_{\rm s}}. \qquad (9)$$

Note that we did not impose any restrictions on the luminosity of the lensing galaxies. If a lens galaxy is much brighter than lensed images, such lens systems may prove difficult to identify from the imaging data alone. This effect becomes particularly important for lensing of faint sources (e.g., Kochanek 1996; Wyithe & Loeb 2002). However, since we are considering cadenced surveys where the strong lens search will make use of differenced survey images (Kochanek et al. 2006), we assume that those systems with bright lensing galaxies can still be successfully identified because the lens galaxy component (as well as any lensed host galaxy light) should be cleanly subtracted. In practice, a bright lens galaxy will act as an additional source of noise; we neglect this here, since many of the surveys we consider are ground-based and will have background-limited images.

2.3 Number density of quasars

We adopt the standard double power-law for the quasar luminosity function. Specifically, we adopt the following parametric form:

$$\frac{d\Phi_{\rm QSO}}{dM} = \frac{\Phi_*}{10^{0.4(\alpha+1)(M-M_*)} + 10^{0.4(\beta+1)(M-M_*)}}. \qquad (10)$$

Here M refers to the absolute i-band magnitude of quasars. We fix the faint end slope of $\beta = -1.45$ and the bright end slope of $\alpha = -3.31$ which was obtained in the combined analysis of the SDSS and 2dF (Richards et al. 2005). At $z > 3$, however, we modify the bright end slope and adopt the shallower slope of $\alpha = -2.58$ which was suggested by observations (Fan et al. 2001).

In addition to this change of slope, we model the redshift evolution of the luminosity function as pure luminosity evolution. Specifically, the break absolute magnitude M_* is described as

$$M_* = -20.90 + 5\log h - 2.5\log f(z), \qquad (11)$$

$$f(z) = \frac{e^{\zeta z}(1 + e^{\xi z_*})}{(\sqrt{e^{\xi z}} + \sqrt{e^{\xi z_*}})^2}, \qquad (12)$$

where the zero-point value of M_*, as well as the normalisation of the luminosity function $\Phi_* = 5.34 \times 10^{-6}h^3$ Mpc^{-3}, is taken from Richards et al. (2005). The parametric form of the redshift evolution, $f(z)$, is taken from Madau et al. (1999) with some modifications to achieve a better match to the observed evolution of the quasar luminosity function. We then determine the values of the parameters ζ, ξ, and z_* to reproduce the quasar luminosity function from $z = 0$ to 5 obtained from the SDSS Data Release 3 (DR3, Richards et al. 2006). We find the best fit values to be $(\zeta, \xi, z_*)=(2.98, 4.05, 1.60)$, which we adopt throughout the paper. In Figure 1, we compare our best-fit luminosity function with the SDSS result of Richards et al. (2006).

In order to convert the i-band absolute magnitude to the apparent magnitude, we need the appropriate K-correction. We adopt that presented by Richards et al. (2006).
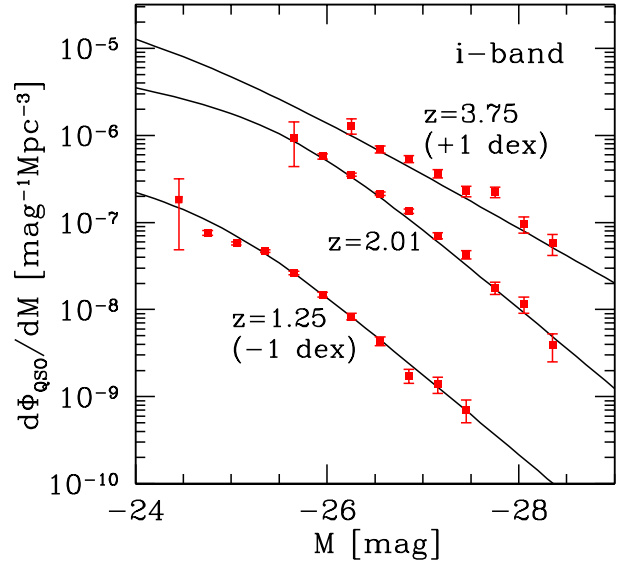

Figure 1. Our model of the i-band quasar luminosity function (eq. [10]), compared with the observed quasar luminosity function from the SDSS DR3 (Richards et al. 2006). We present results at three different redshifts, $z = 1.25$, 2.01, and 3.75, in order to show that our model successfully reproduces the abundance of the SDSS quasars for a wide range of redshifts. Luminosity functions for $z = 1.25$ ($z = 3.75$) are shifted by -1 dex ($+1$ dex) to avoid overlap.

2.4 Number density of supernovae

The rate of occurrence of SNe is closely related to the star formation rate. In this paper we adopt the cosmic star formation rate presented by Hopkins & Beacom (2006),

$$\rho_{\rm SFR}(z) = \frac{(0.0118 + 0.08z)h}{1 + (z/3.3)^{5.2}}[M_\odot{\rm yr}^{-1}{\rm Mpc}^{-3}], \qquad (13)$$

which is essentially the best-fit to the observed star formation rates assuming the initial mass function of Baldry & Glazebrook (2003).

Recent studies of the host galaxies of SNe Ia suggest that delay times ($t_{\rm D}$) of SNe Ia cannot be described by a single value. It has sometimes been assumed that SNe Ia are drawn from two populations, "prompt" (tracing star formation rates) and "old" (tracing stellar masses of host galaxies) SNe (Scannapieco & Bildsten 2005; Mannucci et al. 2005, 2006; Sullivan et al. 2006b; Aubourg et al. 2008). However, such a two-component model may fail to explain the observed low high-redshift SNe Ia rates (e.g., Dahlen et al. 2008). It is naturally expected that more realistic models have widely distributed $t_{\rm D}$, because theoretically the delay time should depend on various parameters such as the mass of the companion star and the metellicity (e.g., Kobayashi & Nomoto 2009, and references therein). In this paper, we use the result of Totani et al. (2008) who constrained the distribution of $t_{\rm D}$ assuming a power-law:

$$f(t_{\rm D}) \propto t_{\rm D}^{-1.08} \quad (t_{\rm D} > 0.1{\rm Gyr}). \qquad (14)$$

Since they found no strong evidence for the presence of the "prompt" ($t_{\rm D} < 0.1$Gyr) component, we do not consider it.
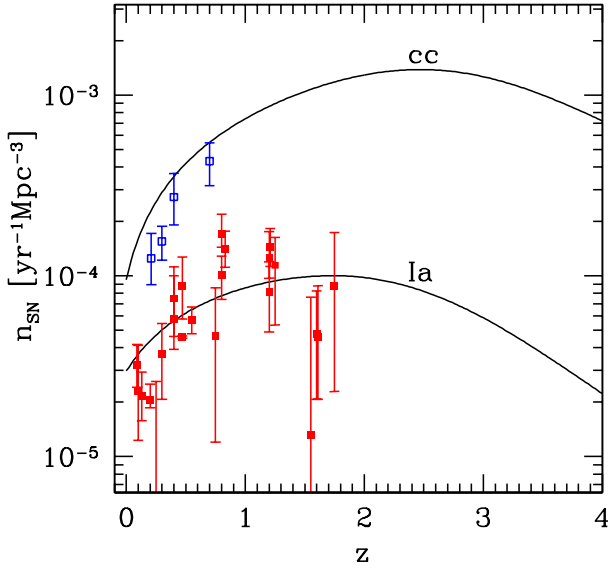
Figure 2. The evolution of SN rates for type-Ia (*lower line*) and core-collapse (i.e., the sum of Ib/c, IIP, IIL, and IIn; *upper line*) SNe adopted in this paper. See text for details of the model. Filled squares are recent measurements of SN Ia rates from Hardin et al. (2000), Pain et al. (2002), Dahlen et al. (2004), Blanc et al. (2004), Neill et al. (2006), Poznanski et al. (2007), Kuznetsova et al. (2008), Botticella et al. (2008), Dilday et al. (2008), Horesh et al. (2008), and Dahlen et al. (2008), whereas open squares are recent measurements of core-collapse SN rates from Dahlen et al. (2004), Botticella et al. (2008), and Bazin et al. (2009). Errors indicate 1σ statistical errors, and do not include any systematic errors.

We can then compute the SN Ia rate as

$$n_{\rm Ia}(z) = \eta C_{\rm Ia} \frac{\int_{0.1}^{t(z)} \rho_{\rm SFR}[z(t - t_{\rm D})] f(t_{\rm D}) dt_{\rm D}}{\int_{0.1}^{t(z=0)} f(t_{\rm D}) dt_{\rm D}}, \qquad (15)$$

The factor $C_{\rm Ia} = 0.032 M_\odot^{-1}$ can be computed from the stellar mass range of $3M_\odot < M < 8M_\odot$ for SNe Ia and the initial mass function of Baldry & Glazebrook (2003). We assume a canonical efficiency of $\eta = 0.04$ (see also Strigari et al. 2005; Hopkins & Beacom 2006).

On the other hand, core-collapse SNe are thought to be related more directly to the star formation rate. They are associated with the death of massive stars whose life time is significantly shorter than the typical cosmological time scale, which suggests that the SN rate of core-collapse SNe is simply proportional to the cosmic star formation rate:

$$n_{\rm cc}(z) = C_{\rm cc} \rho_{\rm SFR}(z), \qquad (16)$$

where $C_{\rm cc} = 0.0132 M_\odot^{-1}$ was derived assuming that core-collapse SNe are produced in the stellar mass range $8M_\odot < M < 50M_\odot$, together with the initial mass function of Baldry & Glazebrook (2003). Following Oda & Totani (2005), we adopt constant relative proportions for four subclasses of core-collapse SNe. Then SN rates are written as

$$n_{\rm X}(z) = f_{\rm X} n_{\rm cc}(z), \qquad (17)$$

where $f_{\rm Ib/c} = 0.23$, $f_{\rm IIP} = 0.30$, $f_{\rm IIL} = 0.30$, and $f_{\rm IIn} = 0.02$ (Dahlén & Fransson 1999). Note that we do not consider SN1987A-like SNe that are very faint compared with

the other core-collapse SNe. Recent analysis suggests that the fraction of type-IIP SNe may actually be much higher (Smartt et al. 2009).

In Figure 2, we compare our model of SN rates with recent measurements. We find that our model is reasonably consistent with the observed SN rates, particularly given the additional systematic errors they involve. The Figure indicates that our model of SN rates is uncertain at the factor of ~ 2 level, suggesting that our predicted numbers of lensed SNe will be similarly uncertain. In particular, our model appears to slightly over-predict the core-collapse SN rate, though it is possible that current observations may miss a fraction of core-collapse SNe given their wide range of intrinsic luminosities. The uncertainty should be even larger at redshift $z \gtrsim 2$ for type-Ia SNe, and $z \gtrsim 1$ for core-collapse SNe, where no measurements of SN rates have been obtained.

We need not only SN rates, but also the brightness distributions of SNe in order to make predictions of the lensed SNe abundance. In what follows the magnitude of SNe refers to the peak magnitude, i.e., the magnitude when the SN is brightest. Again following Oda & Totani (2005), we assume the absolute magnitudes of SNe are Gaussian-distributed (see also Yasuda & Fukugita 2010). With this assumption the luminosity function (in terms of B-band absolute magnitude M) can be written as

$$\frac{d\Phi_{\rm X}}{dM} = \frac{n_{\rm X}(z)}{(1+z)} \frac{1}{\sqrt{2\pi}\sigma_{\rm X}} \exp\left[-\frac{(M - M_{\rm X}^*)^2}{2\sigma_{\rm x}^2}\right], \qquad (18)$$

where $(M_{\rm Ia}^*, M_{\rm Ib/c}^*, M_{\rm IIP}^*, M_{\rm IIL}^*, M_{\rm IIn}^*) = (-19.06, -17.64, -16.60, -17.63, -18.75)$ (for $h = 0.72$) and $(\sigma_{\rm Ia}, \sigma_{\rm Ib/c}, \sigma_{\rm IIP}, \sigma_{\rm IIL}, \sigma_{\rm IIn}) = (0.56, 1.39, 1.12, 0.90, 0.92)$ (Richardson et al. 2002). Note that the luminosity function of SNe (eq. [18]) differs from that of QSOs (eq. [10]) in that the former is in fact the number rate (number per unit time). Thus the factor of $(1+z)^{-1}$ is introduced to account for the cosmological time dilation.

We convert B-band absolute magnitudes to apparent magnitudes in the i-band by computing K-corrections using various SN template spectra. We adopt the spectra at the peak presented by Nugent et al. (2002) for Ia, Levan et al. (2005) for Ib/c, and Gilliland et al. (1999) for IIP, IIL, and IIn.

3 STRONG LENSES IN VARIOUS SURVEYS

In this section, we predict the number of strongly lensed QSOs and SNe for a selection of ongoing and planned surveys, using the model described in detail in §2.

3.1 The expected number of lenses as a function of survey depth

First, we explore how the number of lenses detected increases with survey depth. In Figure 3, we plot the number of lensed QSOs (in a half-sky survey) as a function of i-band limiting magnitude $i_{\rm lim}$. The slope of these number counts is fairly shallow, particularly at $i_{\rm lim} \gtrsim 21$, which suggests that the survey area is much more important than the survey depth when trying to discover many strongly lensed QSOs. The lensing rate is $\sim 10^{-3.5}$, and does not depend very much on
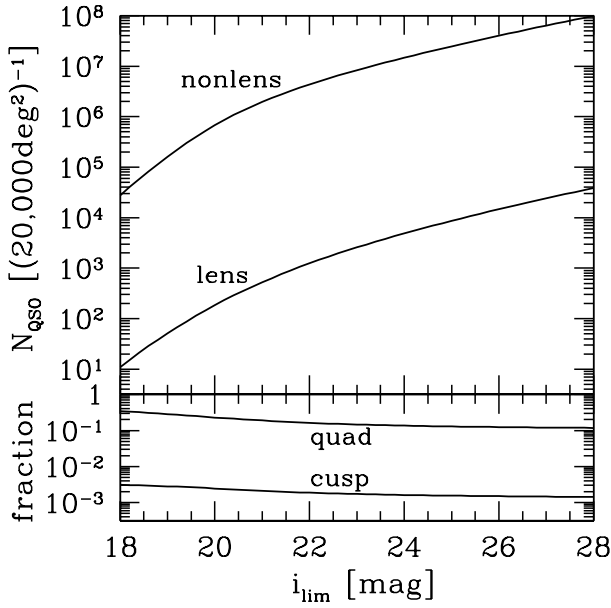
Figure 3. The expected number of lensed QSOs as a function of the *i*-band limiting magnitude i_{lim}. A fiducial survey area of $\Omega = 20,000$ deg^2 is assumed. The number of non-lensed QSOs is also shown for reference. The lower panel shows the ratio of the number of quad (four-images) or naked cusp (three-images) lenses to the total number of lenses, as a function of i_{lim}.

Figure 4. The expected number of lensed SNe as a function of the *i*-band limiting peak magnitude, $i_{\mathrm{peak,lim}}$, for one year monitoring of a fiducial $\Omega = 20,000$ deg^2 survey area. Upper curves indicate numbers of normal unlensed SNe, for reference. Solid lines show expected numbers of SNe Ia, whereas dashed lines show the numbers of core-collapse SNe. The thin lines at > 24 mag show the expected numbers of SNe as a function of $H_{\mathrm{peak,lim}}$ rather than $i_{\mathrm{peak,lim}}$, as relevant for a near-infrared optimised space-based SN survey. The lower panel shows the fractions of quad and naked cusp lenses.

i_{lim} due to the conflicting effects of increasing mean QSO redshift and decreasing magnification bias. We note that the lensing rate is lower than observed in the Cosmic Lens All-Sky Survey (CLASS), $\sim 10^{-2.8}$ (Browne et al. 2003), presumably because of the quite different magnification bias it involves (for instance, in the CLASS the total magnification factor is used for the magnification bias). The recent optical lens survey, the SDSS Quasar Lens Search (SQLS), has obtained a lensing rate of $\sim 10^{-3.3}$, which is more consistent with the calculation above (see Inada et al. 2008). The fraction of quad lenses decreases from $\sim 30\%$ for $i_{\mathrm{lim}} = 18$ to $\sim 10\%$ for $i_{\mathrm{lim}} = 28$, which is roughly consistent with previous calculations (Rusin & Tegmark 2001; Huterer et al. 2005; Oguri 2007b). The small fraction ($\sim 10^{-3}$) of naked cusp lenses indicates that only very wide-field surveys will be able to locate such rare image configurations. We again note that our calculation is applicable only to galaxy scale lenses; naked cusp lenses are much more common at cluster scales, where the radial density profiles of the lenses are shallower (Oguri & Keeton 2004; Minor & Kaplinghat 2008). We also note that our model lens galaxies are all spheroids, with correspondingly low ellipticity. The lower mass, disky lenses, that will make up a small minority ($\lesssim 20\%$, see §2.1) of any survey's yield, may be expected to be more elongated and hence present a higher naked cusp fraction (Keeton & Kochanek 1998).

In Figure 4 we plot the expected numbers of lensed SNe. The slope of the number counts is steeper than it was in the case of the lensed QSOs, suggesting that the survey depth is more important for lensed SNe than it is for lensed quasars. Lensed core-collapse SNe are more abundant than lensed Ia by a factor of several. We find that the fraction of quad systems changes very rapidly as a function of the limiting
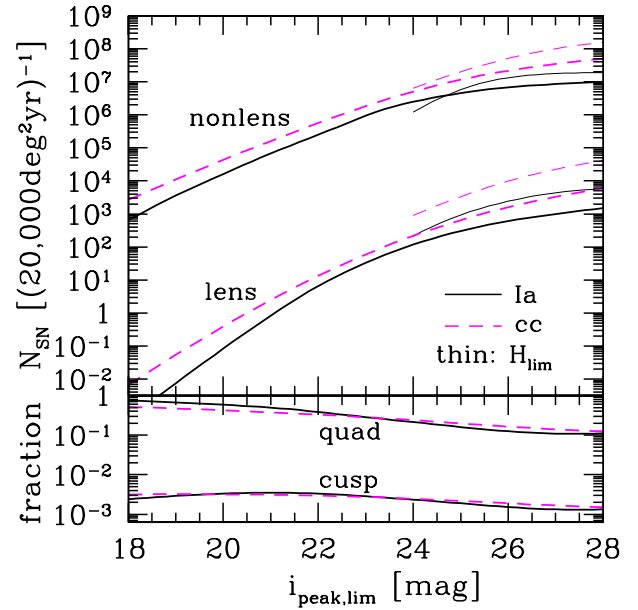
magnitude. For shallow SN surveys, with, say, limiting peak magnitude $i_{\mathrm{peak,lim}} \lesssim 22$, the strong lens sample would be approximately 50% quads. The high quad fraction is due to very large magnification bias inherent to such bright lenses. For deeper surveys of $i_{\mathrm{peak,lim}} \gtrsim 26$, however, the fraction of quad lenses takes a typical value of $10 - 20\%$. The fraction of cusp lenses remains low, $\sim 10^{-3.5}$.

The number of (lensed) SNe does not increase very much beyond $i_{\mathrm{peak,lim}} \sim 24$. This is mainly because of the increasing values of the K-correction at high-redshifts. Since SN spectra have UV cutoff at ~ 3000 Å, the *i*-band K-correction rises quickly at $z \gtrsim 1.7$, which significantly degrades the detectability of such high-redshift SNe in *i*-band images (this effect has long been a source of frustration for ground-based supernova cosmology projects). To illustrate this point, in Figure 4 we also plot the number of SNe as a function of *H*-band limiting peak magnitude, $H_{\mathrm{peak,lim}}$. It is clear that the expected number of lensed SNe is much larger in *H*-band than *i*-band for deep monitoring. The steeper number counts in *H*-band indicates that the effect of K-correction is much less important, illustrating the importance of near-infrared imaging for detecting high-redshift SNe (lensed or otherwise).

3.2 The expected number of lenses in individual surveys

Next we consider strongly lensed QSOs and SNe in several specific time-domain surveys. Each survey is characterised

Table 1. Properties of various time-domain surveys. These are fiducial numbers based on assumptions we describe in the text; given are survey area Ω, 10σ point source limiting magnitude i_{lim} for one visit, one year, and for the final stacked survey image, corresponding assumed median image quality θ_{PSF} (seeing FWHM, in units of arcseconds), cadence (in days), season length t_{season} (in months), survey length t_{survey} (in years) and the effective survey duration $t_{\mathrm{eff}} = t_{\mathrm{survey}} \cdot t_{\mathrm{season}}/12$ (also in years).

Survey	Ω [deg^2]	i_{lim}(visit)	i_{lim}(year)	i_{lim}(total)	θ_{PSF} [arcsec]	cadence [days]	t_{season} [months]	t_{survey} [years]	t_{eff} [years]
SDSS-II	300	21.3	22.9	23.5	1.4	5	3	3	0.75
SNLS	4	24.3	26.3	27.1	0.9	4	5	5	2.1
PS1/3π	30000	21.4	22.2	22.7	1.0	30	2	3	0.5
PS1/MDS	70	23.3	25.2	25.8	1.0	4	6	3	1.5
DES/wide	5000	23.6	24.0	25.1	0.9	30	1	5	0.4
DES/deep	6	24.6	26.1	27.0	0.9	5	3	5	1.3
HSC/wide	1500	24.9	24.9	25.5	0.75	$\ldots^a$	0	3	0.0
HSC/deep	30	25.3	26.6	26.6	0.75	5	2	1	0.2
JDEM/SNAP	15	27.1	$\ldots^b$	29.7	0.14	4	12	1.3	1.3
LSST	20000	23.3	24.9	26.2	0.75	5	3	10	2.5

^{a}The HSC/wide survey is zero cadence: with only one observing epoch per year it would not be suitable for useful lensed SN detection.
^{b}The JDEM/SNAP survey is assumed to be undertaken as a single 1.3 year observing campaign, so does not offer the yearly stack detection strategy. In practice lensed quasars would be detectable simply from the resolved image geometries in any case.

Table 2. The expected numbers of lensed QSOs in various time-domain surveys. The numbers are either for detections only, using stacked images within each survey year, or for well-measured time delays using each visit's image. Some wide-field surveys do not have high enough cadence to measure time delays, and therefore those surveys are useful only for detecting lensed QSOs (see text for more details). We adopt the minimum image separation $\theta_{\mathrm{min}} = (2/3)\theta_{\mathrm{PSF}}$ for all surveys. The numbers of non-lensed QSOs detectable in the surveys are also shown for reference. Percentages in parentheses indicate the fraction of quad lenses.

Survey	QSO (detected)		QSO (measured)	
	N_{nonlens}	N_{lens}	N_{nonlens}	N_{lens}
SDSS-II	1.18×10^5	26.3 (15%)	3.82×10^4	7.6 (18%)
SNLS	9.23×10^3	3.2 (12%)	3.45×10^3	1.1 (13%)
PS1/3π	7.52×10^6	1963 (16%)	$\cdots$	$\cdots$
PS1/MDS	9.55×10^4	30.3 (13%)	3.49×10^4	9.9 (14%)
DES/wide	3.68×10^6	1146 (14%)	$\cdots$	$\cdots$
DES/deep	1.26×10^4	4.4 (12%)	6.05×10^3	2.0 (13%)
HSC/wide	1.76×10^6	614 (13%)	$\cdots$	$\cdots$
HSC/deep	7.96×10^4	29.7 (12%)	4.30×10^4	15.3 (13%)
JDEM/SNAP	5.00×10^4	21.8 (12%)	5.00×10^4	21.8 (12%)
LSST	2.35×10^7	8191 (13%)	9.97×10^6	3150 (14%)

Table 3. The expected number of detected lensed SNe (type Ia and core collapse) in various time-domain surveys. We adopt the minimum image separation $\theta_{\mathrm{min}} = (2/3)\theta_{\mathrm{PSF}}$ for all surveys. The numbers of non-lensed sources detectable in the surveys are also shown for reference. Percentages in parentheses indicate the fraction of quad lenses. For lensed SNe, we adopt the peak magnitude limit of $i_{\mathrm{peak,lim}} = i_{\mathrm{lim}} - 0.7$ in actual calculations so that the lightcurves of lensed SN images can well be traced.

Survey	SN (Ia)		SN (cc)		Note
	N_{nonlens}	N_{lens}	N_{nonlens}	N_{lens}	
SDSS-II	4.34×10^2	0.003 (54%)	1.09×10^3	0.01 (40%)	
SNLS	7.52×10^2	0.03 (24%)	1.44×10^3	0.05 (26%)	
PS1/3π	3.34×10^4	0.28 (53%)	8.23×10^4	0.97 (39%)	detections only
PS1/MDS	2.93×10^3	0.09 (32%)	6.05×10^3	0.16 (30%)	
DES/wide	8.30×10^4	2.7 (29%)	1.62×10^5	4.9 (29%)	detections only
DES/deep	8.95×10^2	0.04 (22%)	1.80×10^3	0.07 (24%)	
HSC/deep	1.10×10^3	0.06 (18%)	2.56×10^3	0.13 (21%)	
JDEM/SNAP^a	1.36×10^4	2.9 (13%)	5.39×10^4	12.0 (18%)	
LSST	1.39×10^6	45.7 (32%)	2.88×10^6	83.9 (30%)	

^{a} Instead of the i-band, we adopt an H-band magnitude limit of $H_{\mathrm{lim}} = 26.8$ to predicted the number of (lensed) SNe, since in practice the detection in space will be done in the near-infrared to optimise the number of high-redshift SN sources.

by the survey area (Ω) and AB magnitude limit $i_{\rm lim}$, defined by the i-band 10σ detection limit for point sources. In some cases, we estimated an approximate 10σ limit from the 5σ detection limit quoted in the reference by subtracting 0.7 mag. In some cases we also made rough conversions between image qualities, in order to represent accurately the conditions currently expected to be achievable. These approximations were confirmed to be accurate at the 5% level using various exposure time calculation tools.[2] For lensed SNe the interpretation of the magnitude limit is not obvious because the brightnesses of SNe change drastically with time. We set the condition that (lensed) SNe will be detected if the peak magnitude is more than 0.7 mag brighter than the magnitude limit of each visit. This requirement is chosen to ensure that the lightcurve of each SN is traced reasonably well, and is consistent with the 25σ peak brightness detection required by Young et al. (2008). In addition, for lensed SNe we need to specify the effective survey duration $t_{\rm eff}$ to predict the total number of lensed SNe. Depending on the survey duration and design, a fraction of lensed SN events may be missed simply because one of the multiple images appears outside the survey time; in this paper we do not consider this "time delay bias" (Oguri et al. 2003) for simplicity. We also adopt different minimum image separation $\theta_{\rm min}$ for different surveys, depending on their typical seeing sizes. Specifically we assume $\theta_{\rm min} = (2/3)\theta_{\rm PSF}$, where $\theta_{\rm PSF}$ is a typical seeing FWHM of each survey, which is empirically consistent with with previous optical lens surveys (e.g., Inada et al. 2008).

Finally, we note that detecting a time-variable lens, and being able to measure its time delay, are two very different things. Since quasars are marked out by their long term variability (e.g., Kelly et al. 2009, Schmidt et al, in preparation), a good strategy for detecting lensed quasars may be to stack images within each survey year, and then look for variability between years. For this reason we consider the limiting magnitude of a survey per year's observation for detecting quasar lenses. Measuring time delays requires dense sampling: we assume that a cadence of < 10 days and a season length of $\geqslant 3$ months are the minimum needed to allow time delay estimation, based on results of previous lens monitoring campaigns (e.g. Fassnacht et al. 2002). We note that quantifying time delay accuracy as a function of photometric precision, season length, and cadence would make a very valuable future study. Detecting *useful* lensed SNe will also require high cadence survey data, since for these lenses there is no option of building up time delay precision in subsequent seasons.

We now briefly describe ongoing and future time-domain surveys which we consider in this paper. Survey parameters for these surveys, including survey areas, limiting magnitudes, and survey durations, are listed in Table 1.

• Sloan Digital Sky Survey-II Supernova Survey (SDSS-II SN). This survey was designed to locate relatively low-redshift ($z \sim 0.05 - 0.35$) supernovae in the so-called "stripe

82" region of the SDSS (Frieman et al. 2008). It involved monitoring an area of 300 deg^2 with five broad-band filters; the limiting magnitude at each epoch is $i_{\rm lim} = 21.3$. The survey consisted of three three-month observing seasons, corresponding to an effective survey duration for the SN search of $t_{\rm eff} = 0.75$ yr. We assume a typical seeing of $1''.4$, and a monitoring cadence of 5 days, giving 18 visits per field per year.

• Supernova Legacy Survey (SNLS). Running for 5 years, with roughly five-month observing seasons for a total effective survey duration of 2.1 years, the SNLS is the cadenced part of the CFHT legacy survey, designed for discovery, classification and monitoring of supernovae at intermediate redshift. The much larger "Wide" part of the survey has only static images that do not (straightforwardly) enable a time delay lens search. The "Deep" fields cover 4 deg^2. In calculating the i-band magnitude limit $i_{\rm lim} = 24.3$, we assumed (constant) median seeing $0''.9$, and 1800s exposure time per epoch (Sullivan et al. 2006a). We also assume a 4-day cadence, leading to 38 visits per field per year.

• Pan-Starrs 1 (PS1). The first 1.8-m telescope of the Pan-STARRS project is carrying out two surveys, the Medium Deep Survey (MDS) and the 3π survey. Both are cadenced, but at different rates. The MDS covers 70 deg^2, and we assume that each of its fields will be observed for three six-month seasons with high (typically 4-day) cadence. We anticipate the 3π survey covering 30,000 deg^2 at lower (typically one month) cadence, and assume three three-month seasons (we follow Young et al. 2008, in anticipating using all the filters in the SN identification). We conservatively assume a median image quality of $1''.0$, and use this to estimate 10σ i-band single-visit limiting magnitudes for each survey of 23.3 (MDS) and 21.4 (3π), extrapolating approximately from the figures given in the design reference mission (Chambers & Dennau 2008).

• Dark Energy Survey (DES). To be carried out with a new wide-field camera installed on the Blanco 4-m telescope at CTIO, this survey, to start in 2012, is also planned to have two components, a wide and a deep (The Dark Energy Survey Collaboration 2005). As with PS1, only the deep fields will have sufficient cadence for time delay estimation, but the wide fields will again allow detection of time-delay lenses by their variability. While the details of the surveys are still being decided, we adopt the following fiducial estimates: a deep survey covering 6 deg^2 for five years (in nearly three-month seasons, with 5-day cadence, giving 16 visits per year), and a wide survey covering 5000 deg^2 for five years, with two observing epochs per year (Frieman 2009). We take the effective season length of the wide survey to be one month, in order to estimate the number of lensed supernovae seen: this is about the period over which 2 images might be simultaneously visible. We assume $i_{\rm lim} = 24.6$ per epoch in the deep fields, and $i_{\rm lim} = 23.6$ per epoch in the wide fields (J. Annis, priv. comm.).

• Hyper Suprime-Cam (HSC). The HSC is a next-generation prime-focus camera for the Subaru 8.2-meter telescope. The field-of-view is 1.5 degree in diameter, and the expected image quality is about $0''.75$ across the entire

---

[2] Specifically, we used the CFHT MegaCam facility "DIET," http://rpm.cfht.hawaii.edu/~megacam/diet/DIET.rpm, and also the LSST ETC at http://dls.physics.ucdavis.edu:8080/etc4_3work/servlets/LsstEtc.html

field-of-view. The survey plan with the HSC is not yet finalised and still very uncertain, but one of the three survey components ("deep") has both area and depth enough to locate many high-redshift supernovae. Here we tentatively assume its survey area to be 30 deg^2 and the limiting magnitude to be $i_{lim} = 25.3$, with a single two month season (which therefore may not be sufficient to measure time delays between multiple images). At an assumed cadence of 5 days, each field would be observed 12 times. Another component (the "wide") may cover 1500 deg^2, with the imaging again being built up one exposure per year, for two or three years. As with PS1/3π and DES/wide, we flag this survey as useful for detection but not time delay measurement. We do not consider the "ultra-deep" survey here as its survey area will be rather small.

• Joint Dark Energy Mission (JDEM). The design of this space-based observatory is still very uncertain, but we can assume that if such a facility is built with high redshift supernovae in mind, it will have an infrared-optimised imager. In this work we compute, as an example, predictions for a JDEM that has indeed been optimised for supernova work, and assume the specifications of the Supernova/Acceleration Probe (SNAP) as our fiducial telescope (Aldering et al. 2004): we assume a 15 deg^2 sky area observed to a depth of $i_{lim} = 27.1$ and $H_{lim} = 26.8$ per epoch at high cadence (4 days) for 1.3 years (where we have again corrected to get 10σ limits). Note that we only consider in this work the SN survey of this strawman JDEM; a weak lensing survey in space should find large numbers of lensed quasars even if the imaging is not cadenced at all, as the single epoch high resolution imaging alone will allow identification of multiple image systems (see, e.g., Kuhlen et al. 2004, for some estimates). However, time delay measurements would be possible only in the SN fields.

• Large Synoptic Survey Telescope (LSST). This 6.7-m effective aperture dedicated survey telescope is designed to survey 20,000 deg^2 of sky for ten years. The "universal cadence" survey outlined by Ivezić et al. (2008) sees each field being observed in 6 filters at typically 5-day cadence in the r and i-bands. A typical field's observing season would last three months or more (with the redder filters sampling a longer season), giving some 20 exposures per field per filter per year. We estimate that the 10σ limiting magnitude in $0''.75$ seeing will be around 23.3, and adopt this as our fiducial single-epoch depth. Ivezić et al. note that "mini surveys" could be carried out with LSST on smaller sky patches to greater depth; we do not consider any such survey here, but note that it would provide higher accuracy time delays on an inevitably smaller number of lenses.

Tables 2 and 3 summarises the expected numbers of lensed QSOs and SNe in each survey. We find that the LSST will find the largest number of lenses with measureable time delays, for both quasars and SNe. The wide surveys of the HSC, DES and PS1 projects will also discover large numbers of lensed quasars thanks to their wide field-of-view, but they will not have sufficient time domain sampling to measure the time delays between quasar images. The corresponding deep surveys, or a spaced-based JDEM/SNAP survey, will provide time delay measurements, but only for ~ 60 lensed quasars, because of their small combined field-of-view. The LSST is unique because it has *both* the wide field-of-view to cover many quasars and the frequent time domain sampling for monitoring of lens systems, allowing us to obtain time delay measurements for ~ 3000 lensed quasars. It will be quite challenging to find lensed SNe in ground-based surveys before LSST, as the expected number of lensed SNe discovered is only ~ 1. In contrast, the very deep monitoring by a JDEM/SNAP survey would allow us to locate ~ 15 lensed SNe in total, despite the relatively small field of view of 15 deg^2. The LSST will also be powerful for detecting lensed SNe; our calculation indicates that the LSST will discover ~ 130 lensed supernovae during its 10-year survey.

4 GENERATING MOCK CATALOGUES: A MONTE-CARLO APPROACH

Here we compute the expected number of strong lenses, and their distributions with lens and source property, in a different way from the standard technique described in §2. Essentially it is a semi-analytic technique based on Monte-Carlo realisations of lens and source populations, and is an extension of the method used in Oguri & Blandford (2009) to predict the all-sky distribution of large Einstein radii produced by massive clusters. In essence, we perform the necessary integrals by Monte-Carlo integration, and keep the sample points drawn from the target distribution. The goal is to produce mock catalogues of lenses for a given survey, which can then be used to investigate the feasibility of various science projects.

4.1 Technique description

The specific procedure is as follows. First we randomly generate a list of sources in a given survey area to a given depth, according to the adopted source luminosity function. To allow for the magnification by strong lensing, the limiting magnitude of the source catalogue needs to be deeper than the actual magnitude limit of the survey. We adopt $3 - 3.5$ mag deeper limit than the survey magnitude limit for generating the source catalogue. This is sufficient, particularly given our use of the fainter image magnification factor in computing the magnification bias. Each source realisation contains information on the redshift and apparent magnitude (without lensing magnification) only. Since we ignore any spatial correlations between sources, the whole source population is characterised just by a surface number density. We then randomly generate a list of lenses according to the model described in §2.1. For each mock lens galaxy, we consider the rectangular region with an area of $[8\theta_{Ein}(max)]^2$, where $\theta_{Ein}(max)$ is given by equation (2) with $D_{ls}/D_s = 1$, randomly distribute source objects using the pre-generated catalogue, and for each source solve the lens equation to see if it is multiply-imaged. Again, the lens equation is solved using the software *glafic* (M. Oguri, in preparation). For multiply-imaged sources, we check whether they satisfy the
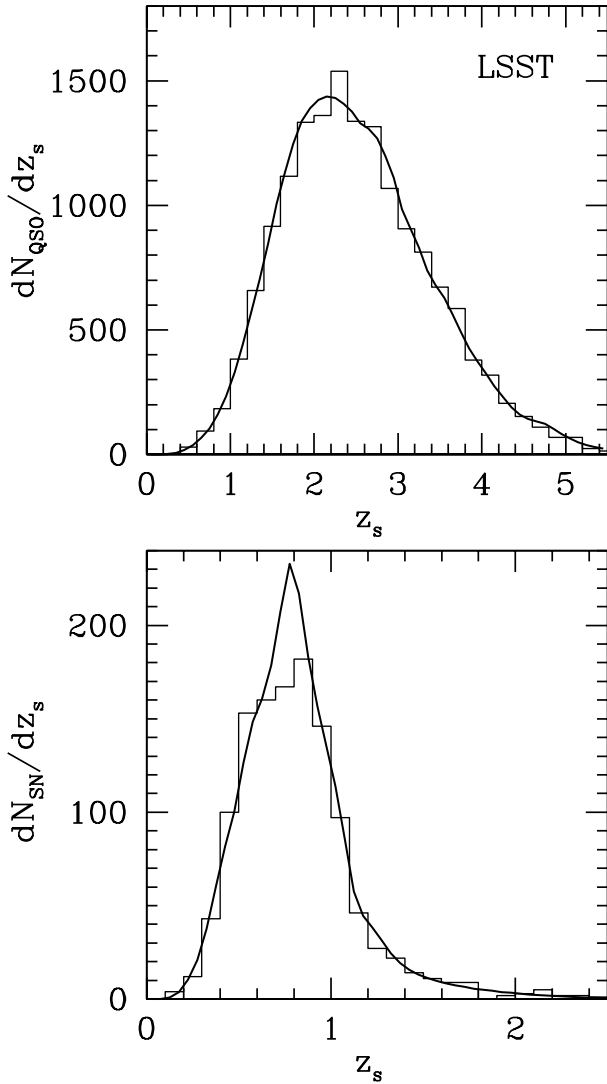
Figure 5. The predicted redshift distributions of lensed QSOs (*upper panel*) and SNe (*lower panel*). The histograms are distributions calculated from the mock lens catalogue constructed using the Monte-Carlo technique, whereas the solid curves are analytic results from equation (7).

Figure 6. Same as Figure 5, but the redshift distributions of lensing galaxies are shown.

detection criteria (the survey limiting magnitude, image separation, and flux ratio), and record only lens systems which survive these criteria. In this way we can generate mock catalogues of lensed sources for a particular survey.

Although the new Monte-Carlo technique tends to be more time-consuming than the traditional analytic approach, it has several important advantages. (1) In this approach we can add more parameters to the lens model with little additional computational cost. In the traditional analytic approach, adding additional lens parameters requires an additional integral, particularly if the distributions of the parameters are not independent of each other. This exponential growth in run time with model complexity is in marked contrast with the Monte-Carlo approach, in which the CPU time required scales approximately linearly with the number of model parameters. (2) It is straightforward to include even quite complicated lens selection functions, e.g., those depen-
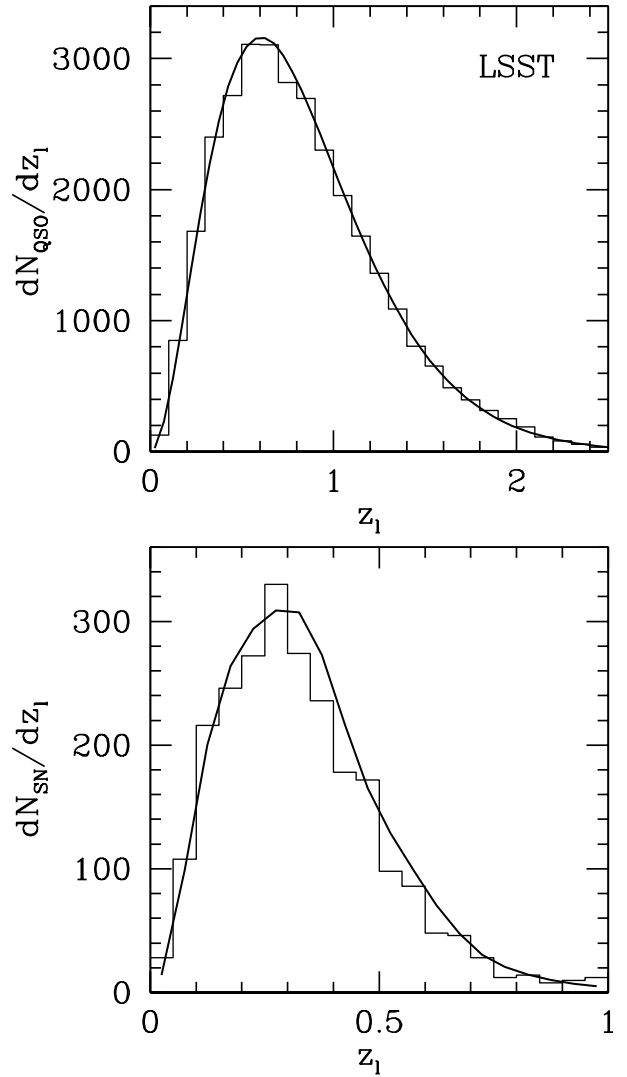
dent on many observables such as flux ratios, image separations, time delays, and the properties of lensing galaxies. (3) From the resulting mock catalogue we can examine the expected distributions of lens and source parameters quite easily. This is important because the population of strong lenses generally differs from the population of general lens and source populations (e.g., Oguri et al. 2005; Möller et al. 2007; Rozo et al. 2007; Mandelbaum et al. 2009), and yet we would very much like to use the former to understand the latter.

4.2 Mock lens catalogue

As a specific example, in this paper we present the mock catalogue of lensed QSOs and SNe expected for the baseline survey planned with LSST (see Table 1 for the survey parameters). In practice, the catalogue is 5 times (QSOs) or 10 times (SNe) over-sampled in order to reduce shot noise. The catalogue contains all the necessary information for each mock lens, including the properties of lenses and sources,
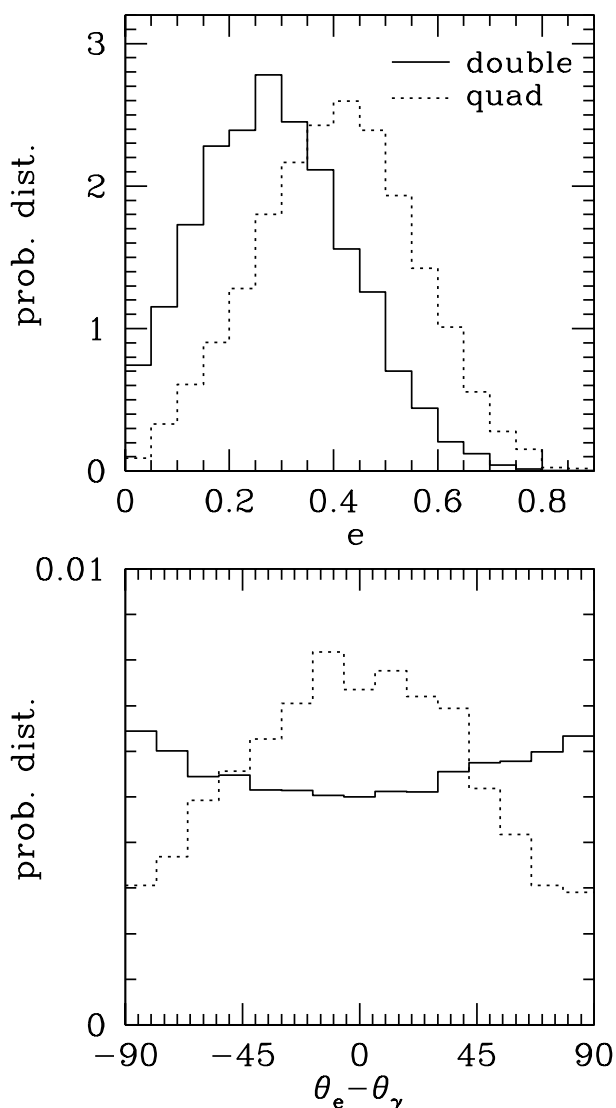
Figure 7. *Upper panel:* The probability distribution of the lens galaxy ellipticity e for double (*solid*) and quad (*dotted*) lenses, obtained from the mock lens catalogue. *Lower panel:* The probability distribution of $\theta_e - \theta_\gamma$, where θ_e is the position angle of the lensing galaxy and θ_γ is the position angle of external shear. Since we assumed random distributions for θ_e and θ_γ, the original unbiased (non-lens) population has a flat distribution of $\theta_e - \theta_\gamma$.

image positions, magnifications, and time delays between image pairs.[3]

First, we examine the redshift distributions, to check the validity of the Monte-Carlo technique. Figure 5 compares the source redshift distribution of the mock lenses with the analytic result obtained from equation (7). The reasonable agreements of the distributions assure us that the Monte-Carlo technique is indeed feasible and reliable. The total number of strong lenses in the mock catalogue is 3132 ± 25 for lensed QSOs and 122 ± 4 for lensed SNe (the errors refer to the 1σ Poisson error), which is again in good agreement

---

[3] The mock lens catalogues described here are available at `http://kipac-prod.stanford.edu/collab/research/lensing/mocklens`

with the analytic result shown in Tables 2 and 3. In Figure 6 we show lens redshift distributions which are again in good agreement.

As discussed above, the mock lens catalogue is useful in studying the lensing bias, i.e., the difference of the lens population from the normal population. As practical examples, in Figure 7 we show the distributions of the lens ellipticity, and of the alignment between the lens galaxy and external shear, for double and quad lenses separately. We find that the lensing galaxies of quad image systems are $\Delta e \sim 0.1$ more elliptical than those of double lenses. This result is broadly consistent with Rozo et al. (2007) who showed such a difference using the analytic approach. It appears that there is no significant difference in the distributions of external shear between double and quad lenses. However, we find that the relative orientation of lensing galaxies and external shear is biased: for quad lenses the direction of external shear is more likely to be aligned with the major axis of the lensing galaxy, whereas for double lenses the direction of external shear is more likely to be aligned with the minor axis. This bias can easily be understood by the well-known approximate degeneracy between galaxy ellipticity and external shear (see, e.g., Keeton et al. 1997).

4.3 Distributions of time delays

The predicted distributions of time delays are important in order to assess the measurability of time delays from future time-domain surveys. In Figure 8 we show the expected distributions of time delays and magnitude differences for strongly lensed image pairs, derived from our LSST mock lens catalogue. For double lenses, typical time delays are $\sim 1 - 3$ months. Lensed SNe have somewhat shorter time delays on average than lensed QSOs, partly because of their lower redshifts and the stronger effect of the magnification bias. In most cases the brighter images arrive first, as is expected from simple spherical mass models, but in some cases the arrival order is inverted, i.e., the fainter images arrive first. In either case the detection of first arrival images is assured because of our use of the fainter image for computing the magnification bias.

For quad lenses the situation is more complicated because there are three independent image pairs. However, in Figure 8 we can clearly see a general trend that the first arrival image tends to be fainter than the second and third arrival images ($\Delta m_{12} > 0$ and $\Delta m_{13} > 0$), and tends to be brighter than the fourth arrival image ($\Delta m_{14} < 0$). Thus we expect that the first image to arrive is most likely the third brightest image; this provides support for our choice of the third brightest images for computing the magnification bias, because it assures the detection of the first lensed SN image to arrive. The appearance of this first SN image close to an early-type galaxy can act as an initial trigger, but two SNe are likely to be needed to confirm the system as a lens (and not a pair of SNe in the lens galaxy itself). The time delay between the first image and the subsequent images will still need to be measured, since the delay between images 2 and 3 will often be very short. Our result indicates that typical time delays for quad lenses range from ~ 1 day for the shortest delay to ~ 1 month for the longest delay.
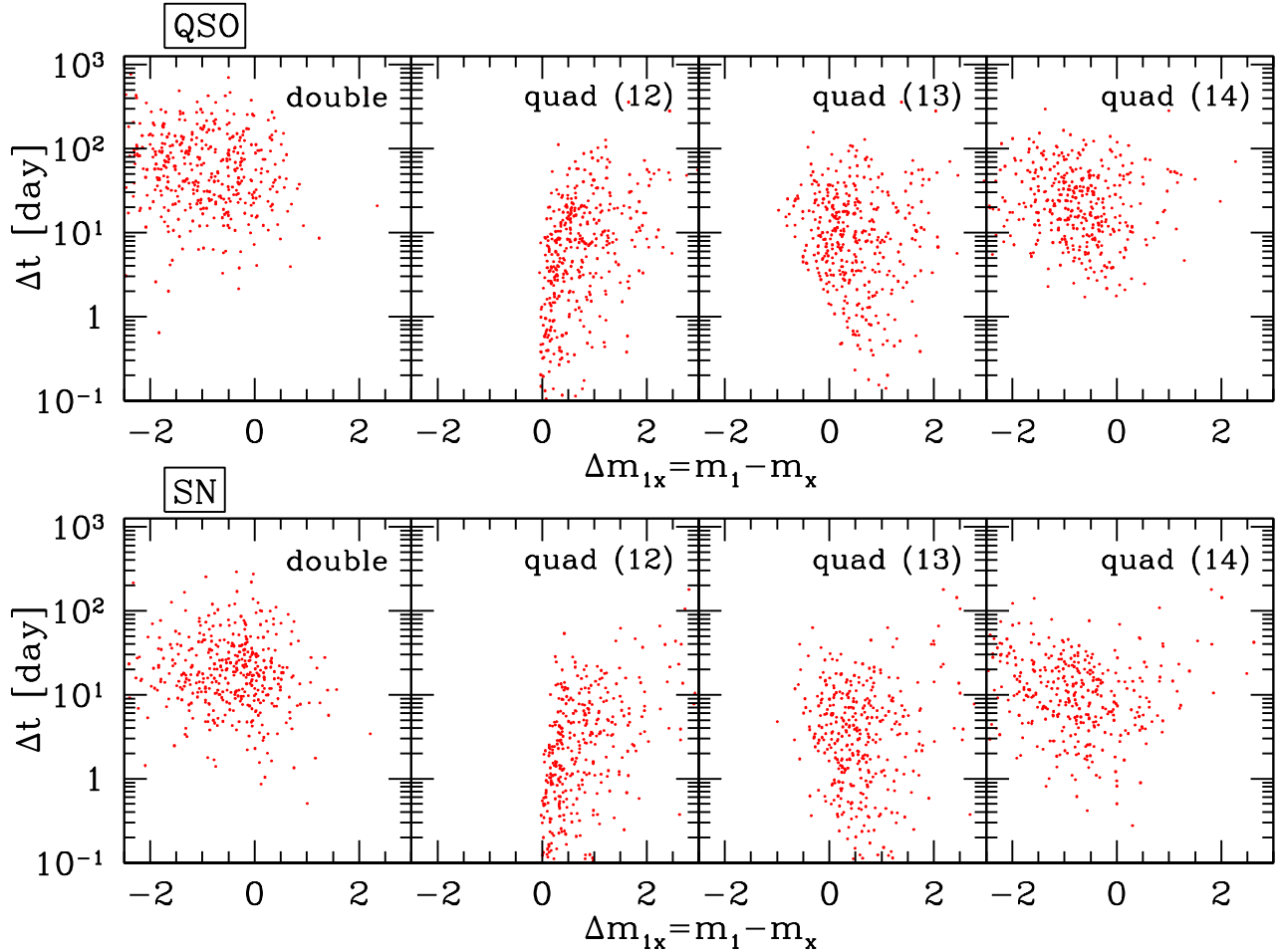
Figure 8. Predicted distributions of time delays and magnitude differences for various image pairs. Each panel shows values for 400 image pairs randomly selected from our mock lens catalogue. Here we name images in order of arrival, i.e., image 1 arrives first, image 2 next, etc. The upper panels show the distributions for lensed quasars, whereas the lower panels are for lensed SNe.

5   COSMOLOGICAL PARAMETERS FROM TIME DELAYS IN LSST

In this section, we use our mock LSST lens catalogue to explore one particular application of a future time-delay lens sample: the measurement of the Hubble constant, and also other cosmological parameters.

5.1   Basic assumptions

We follow the methodology proposed by Oguri (2007a) to combine a number of time delay measurements. The technique was adopted also by Coe & Moustakas (2009) to discuss future constraints from time delays. In brief, we introduce a reduced time delay defined by

$$\Xi \equiv \left| \frac{\Delta t_{ij}}{r_j^2 - r_i^2} \right| \frac{2c}{1 + z_1} \frac{D_{\mathrm{ls}}}{D_{\mathrm{l}} D_{\mathrm{s}}}, \qquad (19)$$

where r_i denotes the distance of image i from the center of the lens galaxy, and study its behavior as a function of the asymmetry $R_{ij} = |r_j - r_i|/|r_j + r_i|$ and the opening angle $\theta_{ij} = \cos^{-1}\left[(\mathbf{x}_i \cdot \mathbf{x}_i)/(r_i r_j)\right]$. While the reduced time delay Ξ becomes unity when the lens potential is exactly

isothermal, external perturbations, non-isothermality, and substructures induce scatter in Ξ.

We construct a subsample of lensed quasars and SNe for our statistical analysis from the mock lens catalogue. First, we restrict the image separation range to $0{\farcs}8 < \theta < 2{\farcs}5$. The upper cut is meant to remove lens systems which are significantly affected by groups/clusters. We do not use lenses with $\theta < 0{\farcs}8$ because the detection and characterisation of lensing galaxies might be difficult for such small-separation lens systems. We also limit the lens redshift to $z_1 < 1.2$ (see also Figure 6), beyond which the 4000Å break of lensing galaxies comes in the z-band and therefore it becomes much more difficult to study the lensing galaxies without deep near-infrared images. Next, for simplicity we consider only the double image lenses that dominate the LSST lens sample. One of the reasons for this is our choice of the third brightest images for computing magnification bias, which suggests that we may not be able to measure some of quad time delays without deeper follow-up monitoring. In either case, our forecast constraints are conservative in the sense that additional quad lenses should only improve the constraints (see also Coe & Moustakas 2009). Finally, we use only lenses with the asymmetry $0.15 < R_{ij} < 0.8$, in which

the effects of various perturbations on Ξ are modest and stable (Oguri 2007a). These cuts leave a sample of 1542 lenses (1476 lensed QSOs and 66 lensed SNe) for our forecast study. The sample has average lens redshift $z_l = 0.65 \pm 0.27$ (where we also give the standard deviation of the sample) and average source redshift $z_s = 2.29 \pm 0.86$ (see also Figure 6), which are reasonably similar to the simple Gaussian distributions assumed in Dobke et al. (2009) and Coe & Moustakas (2009), although it should be kept in mind that these two redshift distributions are not independent but are naturally correlated.

The error on Ξ comes both from measurement uncertainties and from model uncertainties (see Oguri 2007a; Coe & Moustakas 2009). We assume measurement errors of $\sigma(\Delta t) = 2.0$ days and $\sigma(r) = 0''.01$. The assumed time delay measurement error is the same as the one adopted by Coe & Moustakas (2009), which was based on simulations by Eigenbrod et al. (2005). We note that time delay measurements in the optical waveband are complicated by microlensing for both lensed quasars (as Eigenbrod et al. 2005, showed) and lensed supernovae. Dobler & Keeton (2006) discuss the extent to which microlensing can bias time delay measurements in lensed supernovae. While we should be optimistic about achieving 2-day precision given the wealth of additional imaging and spectroscopic data we can anticipate gathering on these precious systems, this is a topic requiring further research.

Based on the Monte-Carlo simulations of (Oguri 2007a), we adopt the model uncertainty of $\sigma(\log \Xi) = 0.08$ which comes mostly from external shear and the scatter in the radial density slope. In this paper, we assume no error on the lens and source redshifts, which corresponds to the situation where all redshifts are measured spectroscopically. See Coe & Moustakas (2009) for the effect of photometric redshift errors on cosmological parameter estimates, which appears to be modest compared with lens potential uncertainties.

As discussed in Oguri (2007a), the main source of systematic error is the unknown mean logarithmic slope of the radial density profile of the lensing galaxies. The parameter $\alpha = \partial \log \phi / \partial \log r$ for each lens is the effective slope of the lens potential, that includes the effect of the external convergence ($\alpha = 1$ corresponds to an effectively isothermal potential, $\phi(\mathbf{x}) \propto r^{\alpha}$). We include the mean slope $\bar{\alpha}$ as an additional nuisance parameter. We include the effect of changing $\bar{\alpha}$ by adopting the scaling relation, $\Xi \propto \Delta t_{ij} \propto (2 - \bar{\alpha})$ (e.g., Refsdal & Surdej 1994; Witt et al. 2000; Wucknitz 2002), and assign it a Gaussian prior. We adopt the fiducial value of $\sigma_{\mathrm{prior}}(\bar{\alpha}) = 0.005$, and marginalise over $\bar{\alpha}$ to obtain constraints on cosmological parameters. We explicitly explore the impact of this assumption in Section 5.3.

5.2 Fisher matrix analysis

We obtain expected constraints on cosmological parameters using the Fisher matrix approach. We compute chi-squared as

$$\chi^2 = \sum_{\mathrm{lens}} \frac{[\log \Xi(z_l, z_s) - \log \Xi_{\mathrm{mock}}]^2}{\sigma(\log \Xi)^2}. \quad (20)$$

Here $\sigma(\log \Xi)$ is the quadratic sum of measurement and model uncertainties. The summation is over the 1542 mock

lenses. Then the Fisher matrix for the parameter set $\{p_1, p_2, \ldots\}$ is calculated as

$$F_{\mu\nu}^{\mathrm{lens}} = \frac{1}{2} \frac{\partial^2 \chi^2}{\partial p_\mu \partial p_\nu}. \quad (21)$$

Here we adopt the standard parametrisation of the dark energy equation of state of the form:

$$w(a) = w_0 + (1 - a)w_{\mathrm{a}}. \quad (22)$$

To complement the strong lensing data, we include the expected constraints from Cosmic Microwave Background (CMB) measurements and distance-redshift relation measurements from (unlensed) type-Ia supernovae. We compute the CMB Fisher matrix $F_{\mu\nu}^{\mathrm{CMB}}$ from upcoming Planck data using the simplified approach described in Mukherjee et al. (2008). In the LSST era, we can expect this to be the basic prior PDF for dark energy studies (Albrecht et al. 2006). For the SNe, we estimate expected constraints from a JDEM/SNAP survey assuming the redshift distribution of SNe in the final subsample given in Aldering et al. (2004). Following Hu et al. (2006), we add 300 local supernovae at $z = 0.05$, and include both statistical and systematic errors in computing the Fisher matrix $F_{\mu\nu}^{\mathrm{SN}}$. In doing so, we include a nuisance parameter, $\mathcal{M}$, which corresponds to the absolute magnitude of type-Ia supernovae, and marginalise over it.

To summarise, assuming a flat universe, we consider the following 8 parameters: $\{w_0, w_{\mathrm{a}}, \Omega_{\mathrm{m}}, h, \bar{\alpha}, \Omega_b h^2, n_s, \mathcal{M}\}$. Note that the time delays depend only on the first 5 of these parameters. Once the Fisher matrices are calculated, we obtain the parameter covariance matrix as $C_{\mu\nu} = (\mathbf{F}^{-1})_{\mu\nu}$, and display the corresponding marginalised constraints as ellipses containing 68% of the probability implied.

5.3 Results

We show the marginalised constraints on the cosmological parameters of interest in Figure 9. We find that the LSST strong lens time delays, combined with the Planck constraints, provide marginalised 1σ uncertainties (68% confidence intervals) of $\sigma(w_0) = 0.15$, $\sigma(w_{\mathrm{a}}) = 0.41$, and $\sigma(h) = 0.017$. If we include the JDEM/SNAP SNe constraints, we obtain $\sigma(w_0) = 0.04$, $\sigma(w_{\mathrm{a}}) = 0.17$, and $\sigma(h) = 0.004$. Although the constraints from time delays are less tight than those from the SNe, time delays still improve the constraint on the dark energy parameters because of the different degeneracy directions. This point is particularly clear in the w_0-h plane, where the two constraints are almost perpendicular with each other. One way to view this is that future supernova surveys can be enhanced by strong lens time delay distance measurements.

We also consider the case where we have a much weaker prior on the mean radial density slope $\bar{\alpha}$: if the prior PDF for this parameter is ten times broader than in our fiducial case, $\sigma_{\mathrm{prior}}(\bar{\alpha}) = 0.05$, the resulting constraints from time delays become much weaker (see Figure 9) and hardly improve future constraints on dark energy from type-Ia SNe. This highlights the importance of accurate prior knowledge on lens potentials when deriving cosmological constraints from time delays. The slight rotation of the ellipse when the prior on $\bar{\alpha}$ is broadened is a result of the time delay dataset
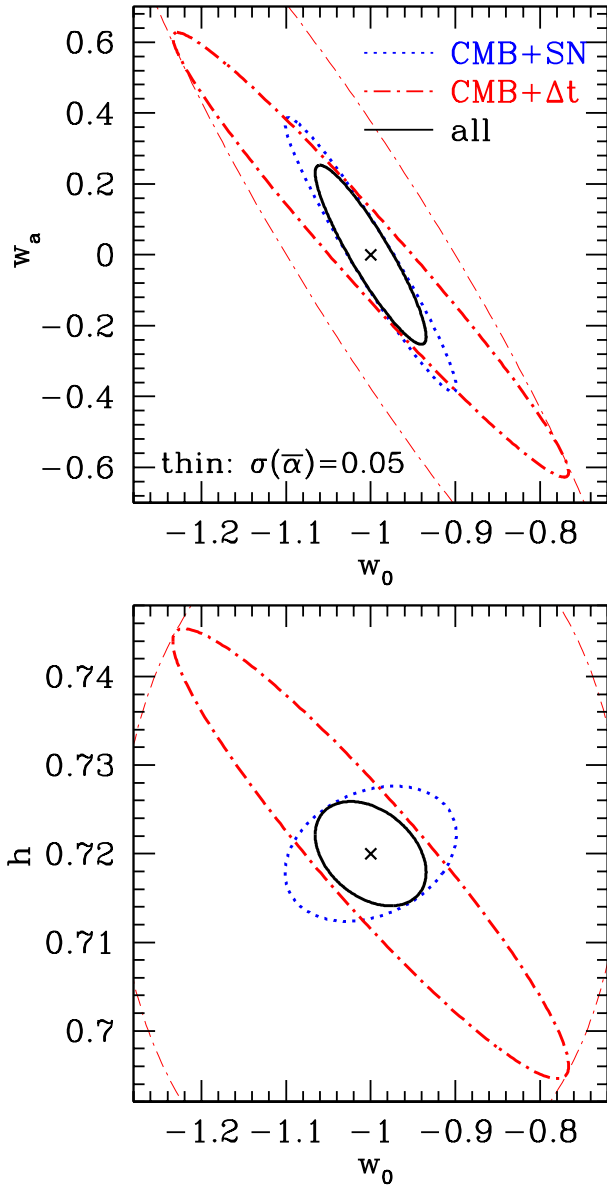
Figure 9. Forecast marginalised constraints in the w_0-w_a plane (*upper panel*) and the w_0-h plane (*lower panel*). Ellipses show 68% confidence regions for various combinations of expected constraints from the Planck satellite (CMB), type-Ia supernovae in SNAP (SN), and time delays in LSST (Δt). Thin ellipses are constraints from CMB+Δt, but assumes a much weaker mean slope prior of $\sigma_{\rm prior}(\bar{\alpha}) = 0.05$ instead of the fiducial value of 0.005.

contributing less strongly to the joint fit – lack of knowledge of the mean density profile slope leads to lensing being downweighted as a cosmological probe.

Indeed, the results presented here depend crucially on the width of the prior on the mean slope, $\sigma_{\rm prior}(\bar{\alpha})$. In Figure 10, we show how the constraints on dark energy are affected by changing $\sigma_{\rm prior}(\bar{\alpha})$. We adopt the standard method of quantifying the constraints on the dark energy parameters, employing the Dark Energy Task Force "figure of merit" (DE FOM), which is proportional to the inverse of the ellipse area in the w_0-w_a plane (Albrecht et al. 2006). We find that time delays would not improve
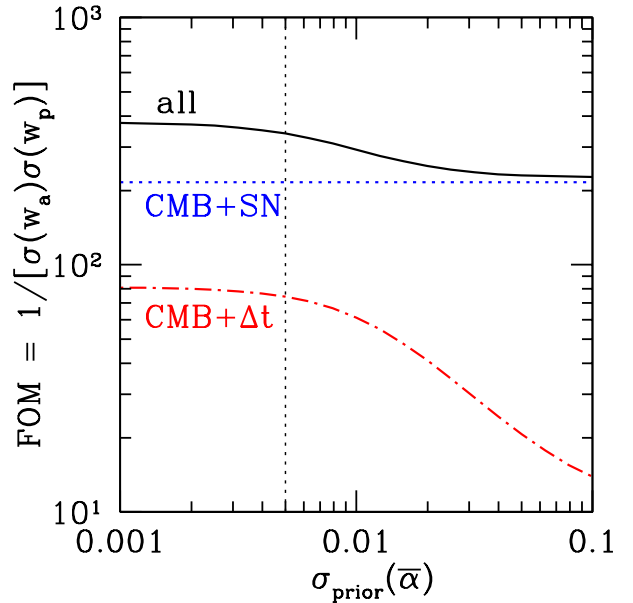

Figure 10. Dark energy figure of merit (FOM; e.g., Albrecht et al. 2006), defined as $1/[\sigma(w_a)\sigma(w_p)]$ with w_p being equation of state at the pivot redshift, as a function of the input (prior) uncertainty on the mean radial lens density profile slope $\bar{\alpha}$. The vertical dotted lines indicate our fiducial prior value, $\sigma_{\rm prior}(\bar{\alpha}) = 0.005$.

upon the constraints from a JDEM/SNAP SNe survey if $\sigma_{\rm prior}(\bar{\alpha}) \gg 0.01$, which suggests that we need to determine the mean radial slope of galaxy density profile to better than ~ 0.01 in order to use time delays in LSST as a future cosmological probe. In the limit of perfect prior information on $\bar{\alpha}$, we see that the LSST time delay sample could improve the DE FOM by a factor of 1.74, from 215 to 375.

6   DISCUSSION

6.1   Static surveys

In this paper, we focused on cadenced surveys, mainly because of the interest in strong lens time delays for use in measuring cosmological parameters, and the promising technique to find such lenses from their time variability (Kochanek et al. 2006). As discussed in §3.2, however, some future wide-field optical imaging surveys will lack sufficient time domain sampling frequency to measure time delays. These surveys will still be useful for locating many lensed quasars, and possibly lensed SNe as well, but they will require extensive follow-up monitoring observations to measure the time delays.

We note that some planned optical imaging surveys will be completely static, i.e., observing each field only once. Previous lens surveys, however, have convincingly shown that we can still identify lensed quasars by checking the colour and morphology of quasars (e.g., Inada et al. 2008). High resolution, space-based surveys will be particularly effective here. For instance, the planned space mission Euclid (Refregier et al. 2010) is planning to obtain high-resolution imaging data for the entire southern extragalactic sky, which will be enormously useful for locating many lensed quasars

from morphology. Once these quasar lens candidates have been identified, follow-up images can be taken to assess the variability of the candidates and to improve the efficiency of lens finding. Again, we will need additional monitoring data in order to measure time delays. Monitoring follow-up of lenses found in static surveys will, however, represent a significant observational undertaking.

6.2 Follow-up observations

Even for well-cadenced surveys such as LSST, we can conduct follow-up monitoring to obtain more accurate time delays. In some cases the survey duration will not be enough to measure long time delays, and for these systems additional monitoring after the survey will be necessary. Particular attention should be paid to the follow-up of strongly lensed SNe because of their transient nature. Clearly it is important to identify lensed SNe as early as possible. In principle it will be possible to trigger follow-up monitoring by the appearance of the first lensed SN image, by checking the difference of photometric redshifts between the SN and its nearby galaxies, or from prior knowledge of the lensed host galaxies. Note that good image position and colour information for SN classification and redshift estimation will be required for this to work. Where these are not available, confirmation of a lensed SN will likely require the appearance of the second image in a lensing configuration.

In our Fisher matrix analysis, we assumed that all the redshifts are known. Spectroscopic redshifts for lensed quasars are relatively easy to obtain, thanks to prominent quasar emission lines. However, we can expect spectroscopy of the lensed SNe and the lensing galaxies to be generally much more difficult, because one has to detect absorption lines to measure the redshifts. Instead, we can adopt photometric redshifts, provided we can cleanly separate the lensed images from the lens galaxy light; if there is no bias inherited in the photometric redshift measurement, its effect is just to degrade the cosmological constraints from the time delays slightly (see Coe & Moustakas 2009). Spectroscopic follow-up observations are also helpful for the confirmation of strong lens systems, although the detection of time delays between the images does itself serve as a strong test of the lensing hypothesis.

6.3 Prospect for constraining lens potentials

One of our main findings (§3.2) is that accurate prior knowledge on lens potentials is crucial for cosmological constraints from time delays. Among others, the most important parameter is the mean slope of the effective radial density profile of the lensing galaxy, $\bar{\alpha}$, including the effect of external convergence. Our requirement of $\bar{\alpha} \lesssim 0.01$ for the LSST time delay sample to be a useful addition to the cosmographic toolbox is in fact not far from the current statistical error of ~ 0.02 from the Sloan Lens ACS Survey (Koopmans et al. 2009). Care will need to be taken to ensure that the LSST lens galaxy sample is similarly well characterised. In addition, we expect that the external convergence may be well modelled by combining photometric information for the surrounding field with ray-tracing in N-body simulations (Oguri et al. 2005; Suyu et al. 2010).

With such a large number of strong lens systems, it may be possible to determine cosmological parameters and the mean radial density slope simultaneously. For instance, Rusin & Kochanek (2005) constrained the mean radial density profile by combining the Einstein radius measurements for lenses with different source redshifts. Moreover, we may also be able to use flux ratios between images to constrain the radial profile (e.g., Mörtsell & Sunesson 2006; Mutka 2010), although we will need to take into account the effects of dark halo substructures, differential dust extinction, and microlensing very carefully. We leave the exploration of these possibilities to future work.

6.4 Comparison with individual lens modelling

While we considered a statistical analysis for combining many time delay measurements, tight cosmological constraints may also be obtained from the detailed modelling of individual lens systems (the so-called "golden lens" approach). Indeed, the feasibility of this has been nicely demonstrated, by e.g. Suyu et al. (2010) for B1608+656 and Fadely et al. (2010) for Q0957+561. One advantage of our statistical approach is that it can handle various perturbations on lens potentials, such as substructures and higher-order external perturbations, more straightforwardly, since their effects average out when combining many lenses. Although the average does not always converge to zero (an example is external convergence), this poses no problems as long as the residual can be predicted reasonably accurately by theory. Indeed, the statistical framework provides a means, in principle, to infer the statistical properties of lens substructure, microlensing and dust simultaneously with the cosmology and lens profile parameters.

For individual modelling we do not need to know the mean radial density profile very accurately, but instead need enough observational constraints to determine the radial profiles of each individual lensing galaxy. For this reason, we expect the quad lenses to be the focus of the individual modelling efforts, complementing the preference for doubles in the statistical approach. To summarise, we expect that individual mass modelling will provide important complementary constraints on cosmological parameters, and help to assess the systematic errors that each methods involves.

6.5 Group- or cluster-scale lenses

Future surveys will discover not only galaxy-scale lenses but also wide-separation lenses produced by massive groups or clusters of galaxies, such as those discovered in the SDSS (Inada et al. 2003, 2006). The time variability information will also be helpful in identifying these lenses as well, but the time delays between images will tend to be long, $\sim 1 - 10$ years for massive clusters, suggesting that well-designed follow-up monitoring program may be necessary to measure their time delays.

7 CONCLUSIONS

We have presented detailed calculations of the likely yields of several planned cadenced surveys, adopting realistic distributions for the lens and source properties, and taking ac-

count of the selection functions, including the magnification bias. We find that, for example, the LSST will discover ~ 8000 lensed quasars (~ 3000 of which will have time delay measurements) and ~ 100 lensed SNe. Approximately one third of lensed SNe will be type-Ia. The lenses are dominated by double (two-image) lenses, with expected quad fractions of $\sim 14\%$ for lensed quasars and $\sim 30\%$ for lensed SNe. We have also produced mock catalogues of lenses, which are useful for probing strong lensing selection effects and the feasibility of various science projects.

We have used a mock catalogue of ~ 1500 well-observed double lenses in LSST to derive expected cosmological constraints. Specifically, we derived precisions on the Hubble constant and the dark energy equation of state parameters from this sample of time delay measurements, assuming priors from Planck. The resulting predicted marginalised 68% confidence intervals are $\sigma(w_0) = 0.15$, $\sigma(w_a) = 0.41$, and $\sigma(h) = 0.017$, implying that time delays can improve constraints from a JDEM supernova type-Ia sample. However, this result holds only if we have accurate prior knowledge of the lens population's mean effective density profile: we find that the prior on the mean radial density slope has to be $\bar{\alpha} \lesssim 0.01$ in order for time delays from the LSST strong lens to be a useful future cosmological probe.

ACKNOWLEDGMENTS

REFERENCES

Albrecht A., et al., 2006, arXiv:astro-ph/0609591
Aldering G., et al., 2004, arXiv:astro-ph/0405232
Aubourg É., Tojeiro R., Jimenez R., Heavens A., Strauss M. A.,Spergel D. N., 2008, A&A, 492, 631
Baldry I. K., Glazebrook K., 2003, ApJ, 593, 258
Bazin G., et al., 2009, A&A, 499, 653
Blanc G., et al., 2004, A&A, 423, 881
Bolton A. S., Burles S., Koopmans L. V. E., Treu T., Gavazzi R., Moustakas L. A., Wayth R., Schlegel D. J., 2008, ApJ, 682, 964
Bonamente M., Joy M. K., LaRoque S. J., Carlstrom J. E., Reese E. D., Dawson K. S., 2006, ApJ, 647, 25
Botticella M. T., et al., 2008, A&A, 479, 49
Browne I. W. A., et al., 2003, MNRAS, 341, 13
Cabanac R. A., et al., 2007, A&A, 461, 813
Chae K.-H., 2003, MNRAS, 346, 746
Chae K.-H., 2007, ApJ, 658, L71
Chambers K. C., Dennau L. J., 2008, PS1 Design Reference Mission, University of Hawaii
Choi Y.-Y., Park C., Vogeley M. S., 2007, ApJ, 658, 884
Coe D., Moustakas L., 2009, ApJ, 706, 45

Coles J., 2008, ApJ, 679, 17
Congdon A. B., Keeton C. R., Nordgren C. E., 2008, MNRAS, 389, 398
Congdon A. B., Keeton C. R., Nordgren C. E., 2010, ApJ, 709, 552
Dahlén T., Fransson C., 1999, A&A, 350, 349
Dahlen T., et al., 2004, ApJ, 613, 189
Dahlen T., Strolger L.-G., Riess A. G., 2008, ApJ, 681, 462
Dalal N., Watson, C. R., 2004, astro-ph/0409483
The Dark Energy Survey Collaboration 2005, arXiv:astro-ph/0510346
Dilday B., et al., 2008, ApJ, 682, 262
Dobke B. M., King L. J., Fassnacht C. D., Auger M. W. 2009, MNRAS, 397, 311
Dobler G., Keeton C. R., 2006, ApJ, 653, 1391
Eigenbrod A., Courbin F., Vuissoz C., Meylan G., Saha P., Dye S., 2005, A&A, 436, 25
Fadely R., Keeton C. R., Nakajima R., Bernstein G. M., 2010, ApJ, 711, 246
Faure C., et al., 2008, ApJS, 176, 19
Fan X., et al., 2001, AJ, 121, 54
Fassnacht C. D., Xanthopoulos E., Koopmans L. V. E., Rusin D., 2002, ApJ, 581, 823
Fukugita M., Futamase T., Kasai M., Turner E. L., 1992, ApJ, 393, 3
Freedman W. L., et al., 2001, ApJ, 553, 47
Frieman J. A., et al., 2008, AJ, 135, 338
Frieman J. A., 2009, talk given at the Santa Fe Cosmology Workshop
Gilliland R. L., Nugent P. E., Phillips M. M., 1999, ApJ, 521, 30
Gavazzi R., Treu T., Rhodes J. D., Koopmans L. V. E., Bolton A. S., Burles S., Massey R. J., Moustakas L. A., 2007, ApJ, 667, 176
Goobar A., Mörtsell E., Amanullah R., Nugent P., 2002, A&A, 393, 25
Goobar A., et al., 2009, A&A, 507, 71
Hardin D., et al., 2000, A&A, 362, 419
Holder G. P., Schechter P. L., 2003, ApJ, 589, 688
Holz D. E., 2001, ApJ, 556, L71
Hopkins A. M., Beacom J. F., 2006, ApJ, 651, 142
Horesh A., Poznanski D., Ofek E. O., Maoz D., 2008, MNRAS, 389, 1871
Hu W., Huterer D., Smith K. M., 2006, ApJ, 650, L13
Huterer D., Keeton C. R., Ma C.-P., 2005, ApJ, 624, 34
Inada N., et al., 2003, Nat, 426, 810
Inada N., et al., 2006, ApJ, 653, L97
Inada N., et al., 2008, AJ, 135, 496
Ivezić Z., et al., 2008, arXiv:0805.2366
Keeton C. R., Kochanek C. S., Seljak U., 1997, ApJ, 482, 604
Keeton C. R., Kochanek C. S., 1998, ApJ, 495, 157
Keeton C. R., Moustakas L. A., 2009, ApJ, 699, 1720
Keeton C. R., 2010, arXiv:0908.3001
Kelly B. C., Bechtold J., Siemiginowska A., 2009, ApJ, 698, 895
Kobayashi C., Nomoto K., 2009, ApJ, 707, 1466
Kochanek C. S., 1991, ApJ, 373, 354
Kochanek C. S., 1996, ApJ, 466, 638
Kochanek C. S., 2002, ApJ, 578, 25
Kochanek C. S., 2006, glsw.conf, 91

Kochanek C. S., Mochejska B., Morgan N. D., Stanek K. Z., 2006, ApJ, 637, L73

Komatsu E., et al., 2009, ApJS, 180, 330

Koopmans L. V. E., Treu T., Bolton A. S., Burles S., Moustakas L. A., 2006, ApJ, 649, 599

Koopmans L. V. E., et al., 2009, ApJ, 703, L51

Kuhlen M., Keeton C. R., Madau P., 2004, ApJ, 601, 104

Kuznetsova N., et al., 2008, ApJ, 673, 981

Levan A., et al., 2005, ApJ, 624, 880

Lewis G. F., Ibata R. A., 2002, MNRAS, 337, 26

Linder E. V., 2004, PhRvD, 70, 043534

Madau P., Haardt F., Rees M. J., 1999, ApJ, 514, 648

Mandelbaum R., van de Ven G., Keeton C. R., 2009, MNRAS, 398, 635

Mannucci F., Della Valle M., Panagia N., Cappellaro E., Cresci G., Maiolino R., Petrosian A., Turatto M., 2005, A&A, 433, 807

Mannucci F., Della Valle M., Panagia N., 2006, MNRAS, 370, 773

Marshall P., Blandford R., Sako M., 2005, NewAR, 49, 387

Minor Q. E., Kaplinghat M., 2008, MNRAS, 391, 653

Mitchell J. L., Keeton C. R., Frieman J. A., Sheth R. K., 2005, ApJ, 622, 81

Möller O., Kitzbichler M., Natarajan P., 2007, MNRAS, 379, 1195

Mörtsell E., Dahle H., Hannestad S., 2005, ApJ, 619, 733

Mörtsell E., Sunesson C., 2006, JCAP, 1, 12

Mukherjee P., Kunz M., Parkinson D., Wang Y., 2008, PhRvD, 78, 083529

Mutka P. T., 2010, arXiv:0909.2168

Myers S. T., et al., 2003, MNRAS, 341, 1

Neill J. D., et al., 2006, AJ, 132, 1126

Nugent P., Kim A., Perlmutter S., 2002, PASP, 114, 803

Oda T., Totani T., 2005, ApJ, 630, 59

Oguri M., 2006, MNRAS, 367, 1241

Oguri M., 2007a, ApJ, 660, 1

Oguri M., 2007b, NJPh, 9, 442

Oguri M., et al., 2008, AJ, 135, 512

Oguri M., Blandford R. D., 2009, MNRAS, 392, 930

Oguri M., Kawano Y., 2003, MNRAS, 338, L25

Oguri M., Keeton C. R., 2004, ApJ, 610, 663

Oguri M., Keeton C. R., Dalal N., 2005, MNRAS, 364, 1451

Oguri M., Suto Y., Turner E. L., 2003, ApJ, 583, 584

Pain R., et al., 2002, ApJ, 577, 120

Pindor B., 2005, ApJ, 626, 649

Porciani C., Madau P., 2000, ApJ, 532, 679

Poznanski D., et al., 2007, MNRAS, 382, 1169

Refregier A., Amara A., Kitching T. D., Rassat A., Scaramella R., Weller J., Euclid Imaging Consortium f. t., 2010, arXiv:1001.0061

Refsdal S., 1964, MNRAS, 128, 307

Refsdal S., Surdej J., 1994, RPPh, 57, 117

Richards G. T., et al., 2005, MNRAS, 360, 839

Richards G. T., et al., 2006, AJ, 131, 2766

Richardson D., Branch D., Casebeer D., Millard J., Thomas R. C., Baron E., 2002, AJ, 123, 745

Riess A. G., et al., 2009, ApJ, 699, 539

Rozo E., Chen J., Zentner A. R., 2007, arXiv:0710.1683

Rusin D., Kochanek C. S., 2005, ApJ, 623, 666

Rusin D., Ma C.-P., 2001, ApJ, 549, L33

Rusin D., Tegmark M., 2001, ApJ, 553, 709

Saha P., Williams L. L. R., 2003, AJ, 125, 2769

Saha P., Coles J., Macciò A. V., Williams L. L. R., 2006, ApJ, 650, L17

Scannapieco E., Bildsten L., 2005, ApJ, 629, L85

Schechter P. L., 2005, IAUS, 225, 281

Smartt S. J., Eldridge J. J., Crockett R. M., Maund J. R., 2009, MNRAS, 395, 1409

Stanishev V., et al., 2009, A&A, 507, 61

Strigari L. E., Beacom J. F., Walker T. P., Zhang P., 2005, JCAP, 4, 17

Sullivan M., et al., 2006a, AJ, 131, 960

Sullivan M., et al., 2006b, ApJ, 648, 868

Suyu S. H., Marshall P. J., Auger M. W., Hilbert S., Blandford R. D., Koopmans L. V. E., Fassnacht C. D., Treu T., 2010, ApJ, 711, 201

Totani T., Morokuma T., Oda T., Doi M., Yasuda N., 2008, PASJ, 60, 1327

Treu T., Koopmans L. V. E., 2004, ApJ, 611, 739

Turner E. L., Ostriker J. P., Gott J. R., III, 1984, ApJ, 284, 1

Walsh D., Carswell R. F., Weymann R. J., 1979, Nature, 279, 381

Witt H. J., Mao S., 1997, MNRAS, 291, 211

Witt H. J., Mao S., Keeton C. R., 2000, ApJ, 544, 98

Wucknitz O., 2002, MNRAS, 332, 951

Wyithe J. S. B., Loeb A., 2002, ApJ, 577, 57

Yasuda N., Fukugita M., 2010, AJ, 139, 39

York D. G., et al., 2000, AJ, 120, 1579

Young D. R., Smartt S. J., Mattila S., Tanvir N. R., Bersier D., Chambers K. C., Kaiser N., Tonry J. L., 2008, A&A, 489, 359